PCCP

ROYAL SOCIETY OF CHEMISTRY

PAPER

View Article Online
View Journal | View Issue

Cite this: *Phys. Chem. Chem. Phys.*, 2024, **26**, 8287

How space-charge behaviour at grain boundaries in electroceramic oxides is modified by two restricted equilibria†

A. L. Usler, * F. Ketter and R. A. De Souza

Received 1st December 2023,
Accepted 8th February 2024

DOI: 10.1039/d3cp05870k

rsc.li/pccp

Determining the space-charge potential at grain boundaries in oxides by various experimental methods bears the promise of providing a comprehensive, quantitative description of interfacial defect chemistry. In this study, we draw attention to the problem of unifying data measured in different temperature ranges. We focus on unifying data from elevated-temperature electrical methods, such as impedance spectroscopy and current–voltage measurements, with data from room-temperature imaging techniques, such as Scanning Probe Microscopy (SPM), Transmission Electron Microscopy (TEM), and Atom Probe Tomography (APT). By means of continuum simulations, we calculate the space-charge potential Φ_0 at grain boundaries in the model electroceramic oxide acceptor-doped $SrTiO_3$, taking into account, first, a restricted equilibrium that leads to frozen-in acceptor-dopant profiles, and subsequently, a restricted equilibrium that leads to frozen-in bulk oxygen-vacancy concentrations. Our results indicate non-trivial differences between experimental values of Φ_0 obtained from electrical and from imaging methods, differences that arise from the different measurement temperatures and that are aggravated by the restricted equilibria. We also show that grain-boundary widths determined from elemental acceptor-cation profiles will not, on principle, agree with the electrical width extracted from impedance spectroscopy data.

1 Introduction

Grain boundaries are regions of perturbed lattice structure. Although the volume fraction of such regions may be very small, their presence in electroceramic oxides can influence, if not govern, the materials' overall behaviour. In polycrystalline samples of the model electroceramic oxide[1] $SrTiO_3$, for example, grain boundaries change the material's plasticity,[2,3] alter its superconductive properties,[4,5] give rise to varistor behaviour,[6–8] facilitate resistive switching,[9] and strongly increase its electrical resistance.[7,8,10–16] The latter effect in particular is characteristic of grain boundaries across a variety of ionic and mixed ionic–electronic conducting electroceramics, such as systems based on CeO_2,[17–20] ZrO_2,[19,21–23] $LaGaO_3$,[24,25] $BaZrO_3$,[26–30] and $BaCeO_3$.[31,32]

The high grain-boundary resistance in acceptor-doped $SrTiO_3$ is commonly explained by the presence of attendant space-charge layers.[7,11,12,33–35] Specifically, the grain boundaries are assumed to exhibit an excess positive charge that is compensated by adjacent negative space-charge layers in which the mobile positive charge carriers (oxygen vacancies and electron holes) are depleted. Such models readily explain why the grain-boundary effect persists in the absence of impurity phases.[7,11,15,36–38] In addition, they predict that oxygen diffusion is hindered at grain boundaries;[39,40] they explain why, at grain boundaries, oxide-ion currents are hindered more strongly than electronic currents;[41,42] they predict the conductivity changes upon reduction to the nanoscale;[38,43–46] and they can account for the varistor behaviour of $SrTiO_3$ ceramics.[7,8,47]

The strength of a space-charge effect is typically quantified by the space-charge potential Φ_0, that is, the difference in the electric potential between the grain boundary and the bulk. Electrical measurements yield Φ_0 most easily from the ratio of the grain-boundary and bulk time constants[14] obtained by means of impedance spectroscopy. It has also been proposed that Φ_0 may be calculated from the nonlinearity of the current–voltage curve.[48–50] A second characteristic of space-charge layers is their extent, ℓ_{gb}. In particular, the electrical grain-boundary width can be extracted from the ratio of grain-boundary and bulk capacitances obtained by impedance spectroscopy.

Imaging techniques can not only provide estimates of Φ_0 and ℓ_{gb}, but also, in comparison with the electrical methods,

Institute of Physical Chemistry, RWTH Aachen University, 52056 Aachen, Germany. E-mail: usler@pc.rwth-aachen.de, desouza@pc.rwth-aachen.de

† Electronic supplementary information (ESI) available. See DOI: https://doi.org/10.1039/d3cp05870k

direct access to the spatial profiles of the electric potential and of elemental concentrations. Scanning probe microscopy (SPM),[51,52] for example, can be used to probe the electric potential profile across a grain boundary. Atom probe tomography (APT) measurements can provide an atomic-scale imaging of a grain boundary's chemical composition,[53–55] from which the space-charge density can be obtained (and thus the space-charge potential). In transmission electron microscopy (TEM), various techniques are available for characterising grain-boundary space-charge layers: electric potential profiles may be calculated from the transmitted electrons' phase shift (electron holography);[56–59] local electric fields can be probed by monitoring the electron beam's deflection in differential phase-contrast (DPC) imaging;[60–62] and dopant concentration profiles across grain boundaries can be obtained, *e.g.*, by electron energy loss spectroscopy (EELS). Such results will generally be obtained, however, for one specific grain boundary and may, therefore, not be representative of all grain boundaries in a ceramic sample.[36,63] Nevertheless, the results from SPM,[64] DPC,[62] and EELS[65–67] measurements are qualitatively consistent with a positive electric potential barrier at grain boundaries in acceptor-doped $SrTiO_3$ bicrystals.

Various sources of errors in the extraction of either Φ_0 or ℓ_{gb} have been discussed in the literature, both for electrical[68–73] and for imaging[67,74–77] techniques. But regardless of these technical shortcomings, a fundamental issue sets the results apart: the different experimental techniques operate in different temperature ranges. Electrical measurements are typically conducted at elevated temperatures (>500 K), while imaging techniques are typically applied at room temperature or below. While different temperature intervals are not problematic *per se*, they do constitute a problem when they are confined to different defect-kinetics regimes. Simple extrapolation of data from one temperature interval to another then becomes non-trivial. Two aspects are particularly important in that regard: first, the acceptor cations' migration is frozen-in at some temperature (between 1000 K and 1300 K in $SrTiO_3$, depending on the cooling rate), such that the accumulation profile is frozen-in (see Fig. 1a); second, the oxygen surface-exchange reaction becomes kinetically hindered[78] at some temperature (between 550 K and 750 K in $SrTiO_3$, again depending on the cooling rate), such that the oxygen-vacancy content of a sample is frozen-in (see Fig. 1b). NB: the oxygen-vacancy mobility may still be appreciable down to much lower temperatures;[78] in fact, the room-temperature conductivity in acceptor-doped $SrTiO_3$ is predominantly ionic.[79–81] When space-charge properties are probed in different temperature ranges, the outcomes must, therefore, be expected to differ, and the same is true for samples that have been subjected to different heat treatments. A sample that is cooled down slowly will generally reach equilibrium (chemical or electrochemical) down to lower temperatures than a sample that is quenched rapidly. The first of these two restricted equilibria, frozen-in acceptor profiles in space-charge zones, has been recognised for diverse electroceramic oxides.[19,33,35,72,73,82–85] The second, negligible oxygen exchange, has been considered quantitatively

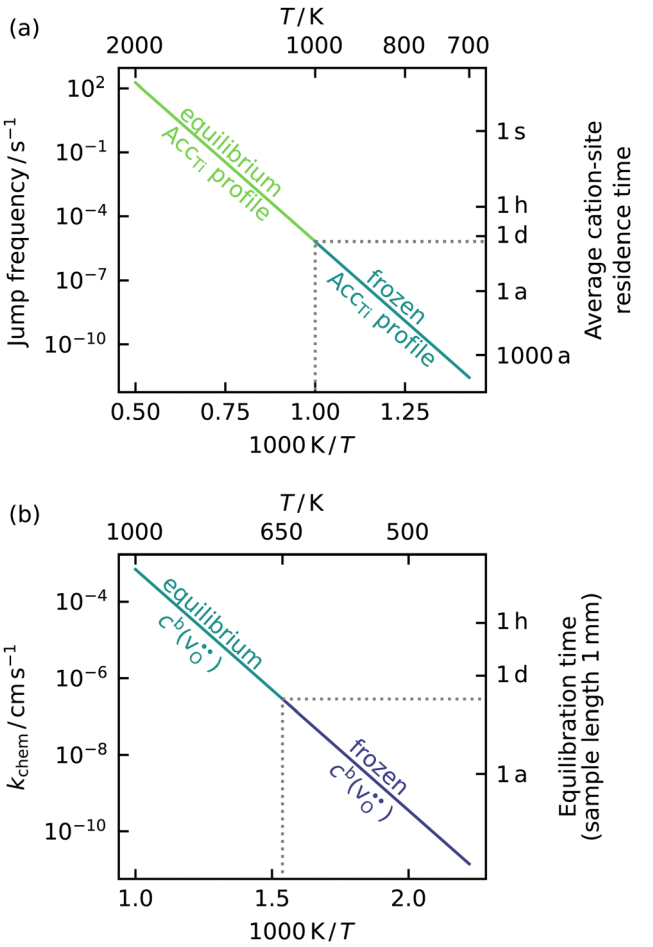

Fig. 1 Illustrative considerations of two restricted equilibria: (a) we take the average cation residence time as a proxy for the time for the acceptor-dopant profile in a space-charge region to come to equilibrium. We calculate, therefore, the jump frequency at a field strength, and from this, the residence time. The jump frequency for $Sr_{Sr}^{\times}$ was calculated from diffusion data,[95] taking into account both the enhanced v_{Sr}'' concentration in the space-charge layer (given Φ_0 = 0.5 V) and the acceleration of transport by the space-charge layer's inherent electric field (assuming a field strength of $|E|$ = 1 MV cm^{-1}).[96,97] (b) We estimate the chemical equilibration time for a sample of 1 mm thickness on the basis of surface-exchange coefficients k^{δ} from ref. 40.

in bulk defect-chemical models of diverse electroceramic oxides;[27,78,86–94] it has not been included, however, in models of interfacial defect chemistry.

In this study, we examine the effects of the two above-mentioned, consecutive restricted equilibria on grain-boundary space-charge layers in acceptor-doped $SrTiO_3$ by means of continuum simulations. First, we discuss in a general way how space-charge properties evolve with decreasing temperature. By inspecting the dependence of Φ_0 on the temperature, we then demonstrate the differences that can arise when Φ_0 values gathered at different temperatures are compared, and we assess the influence of different thermal histories on Φ_0. Finally, we estimate different measures of a grain-boundary width (chemical and electrical) from our simulations and discuss their differences.

2 Modelling

The simulations were implemented in Python. Equations for the bulk defect chemistry were solved with standard routines from the SciPy package.[98] The space-charge layers were simulated by means of the Finite Element Method (FEM), with the FEniCS package.[99–102] Data analysis was carried out with the NumPy,[103] SciPy,[98] and Matplotlib[104] packages.

2.1 Bulk defect chemistry

The bulk defect chemistry of acceptor-doped $SrTiO_3$ is (at moderate pO_2 and not too high T) determined by oxygen vacancies ($v_O^{\bullet\bullet}$), electrons and electron holes (e' and $h^\bullet$), and acceptor cations, both ionised and neutral (Acc'_{Ti} and $Acc^\times_{Ti}$).[78,79,105,106] The bulk concentrations (c^b) of these defects are subject to the constraints of electroneutrality,

$$c^b(h^\bullet) + 2c^b(v_O^{\bullet\bullet}) - c^b(e') - c^b(Acc'_{Ti}) = 0, \quad (1)$$

and of mass conservation of the acceptor dopant,

$$c^b(Acc'_{Ti}) + c^b(Acc^\times_{Ti}) - c^b(Acc_{Ti}) = 0, \quad (2)$$

where $c^b(Acc_{Ti})$ denotes the bulk doping level. The relationships between the defect concentrations are described by three defect equilibria

$$O_O^\times \rightleftharpoons v_O^{\bullet\bullet} + \frac{1}{2}O_2 + 2e' \quad (3)$$

$$\text{nil} \rightleftharpoons e' + h^\bullet \quad (4)$$

$$Acc^\times_{Ti} \rightleftharpoons Acc'_{Ti} + h^\bullet. \quad (5)$$

The equilibrium bulk defect concentrations are obtained by solving the corresponding mass-action laws:

$$c^b(v_O^{\bullet\bullet})p(O_2)^{1/2}c^b(e')^2 = K_{red} \quad (6)$$

$$c^b(e')c^b(h^\bullet) = K_{eh} \quad (7)$$

$$\frac{c^b(Acc'_{Ti})c^b(h^\bullet)}{c^b(Acc^\times_{Ti})} = K_{ion}, \quad (8)$$

with the equilibrium constants being described as temperature-dependent functions:[107,108]

$$\frac{K_{red}}{cm^{-9}\ bar^{1/2}} = 6.616 \times 10^{68} \cdot \exp\left(-\frac{5.581\ eV}{k_B T}\right) \quad (9)$$

$$\frac{K_{eh}}{cm^{-6}} = 7.49 \times 10^{45} \cdot \exp\left(-\frac{3.459\ eV}{k_B T}\right) \quad (10)$$

$$\frac{K_{ion}}{cm^{-3}} = 2.71 \times 10^{25} \cdot \exp\left(-\frac{1.35\ eV}{k_B T}\right). \quad (11)$$

These values are characteristic for $SrTiO_3$: a reduction enthalpy between 5.2 eV and 6.1 eV,[105,108–111] an effective bandgap of 3.4 eV (which includes the temperature dependence of the effective densities of states),[108,112] and charge-transition levels of ~1 eV for acceptor cations (*e.g.*, Fe, Al) in titanate perovskites.[34,78,79,107,110,113–115]

Below the critical temperature T_{crit}^{surf}, the oxygen surface-exchange reaction is assumed to be (abruptly) kinetically hindered, such that the oxygen-exchange equilibrium, eqn (3), can no longer be attained. The restricted chemical equilibrium below this temperature is described by solving together eqn (1), (2), (7) and (8), while keeping the oxygen-vacancy concentration fixed at its equilibrium value from $T = T_{crit}^{surf}$.

2.2 Space-charge layers

Space-charge layer formation in acceptor-doped $SrTiO_3$ is assumed[35,116,117] to be due to a difference in the oxygen vacancies' standard chemical potential between the grain-boundary core and the bulk phase ($\Delta\mu_v^\ominus < 0$), an assumption supported by the results of atomistic simulations.[118–120] This driving energy leads to $v_O^{\bullet\bullet}$ segregating to the grain-boundary core, and thus, to the buildup of an excess positive core charge. Defect–defect interactions are neglected in our model, and hence, $\Delta\mu_v^\ominus$ is assumed to be independent of the defect concentrations within the core. Non-zero driving energies for other point defects are possible (within certain bounds[35]), but for simplicity, they are set to zero. This means that changes in the concentrations of other mobile defects can only occur in response to the electrical field that develops through the redistribution of the oxygen vacancies. The electrostatics of the system are described by the Poisson equation:

$$-\varepsilon_r\varepsilon_0\frac{d^2\phi}{dx^2} = e \cdot \left(c(h^\bullet) + 2c(v_O^{\bullet\bullet}) - c(e') - c\left(Acc'_{Ti}\right)\right). \quad (12)$$

The relative dielectric permittivity of $SrTiO_3$, ε_r, is a function of temperature, conforming to Curie–Weiss behaviour.[121–126] Specifically, we describe $\varepsilon_r(T)$ with[121]

$$\varepsilon_r(T) = \frac{90\,000\ K}{T - 35\ K}. \quad (13)$$

We treat the ionic defects as structural elements (*e.g.*, $O_O^\times$ and $v_O^{\bullet\bullet}$), rather than as building units[127] (*e.g.*, $\{v_O^{\bullet\bullet} - O_O^\times\}$), both in the bulk and in the grain boundary.[35] Consequently, their concentrations must be coupled explicitly with a set of constraints. The ionic defects are subject to site-exclusion constraints that describe the impossibility of a lattice site's double occupation:

$$c(v_O^{\bullet\bullet}) + c(O_O^\times) = \gamma_O \quad (14)$$

$$c(Acc'_{Ti}) + c(Acc^\times_{Ti}) + c(Ti^\times_{Ti}) = \gamma_{Ti}, \quad (15)$$

where γ_O and γ_{Ti} are the site densities of the oxygen and titanium sublattices. These densities are calculated from the lattice parameter a:

$$\gamma_{Ti} = \frac{1}{3}\gamma_O = a^{-3}, \quad (16)$$

with a being obtained as a function of temperature T according to[97]

$$a/Å = 3.90 + 6.64 \times 10^{-5}\ K^{-1} \cdot T. \quad (17)$$

We assume that the grains are large enough for the bulk to be unaffected by concentration changes (*i.e.*, acceptor-dopant accumulation) in the space-charge layers. All bulk concentrations are, therefore, approximated as constant.

Electrons, holes, and oxygen vacancies attain electrochemical equilibrium within the solid under all considered conditions. The acceptor cations are assumed to attain electrochemical equilibrium above $T_{\mathrm{crit}}^{\mathrm{cat}}$ (this is also called the Gouy–Chapman case[128,129]); for $T < T_{\mathrm{crit}}^{\mathrm{cat}}$, the redistribution of acceptor cations is modelled as being frozen-in. Possible defect–defect interactions are ignored, so that the defect concentrations in the space-charge layers can be expressed in standard Maxwell–Boltzmann forms:

$$c(\mathrm{h}^{\bullet}) = c^{\mathrm{b}}(\mathrm{h}^{\bullet})\cdot \mathrm{e}^{-\alpha\phi} \tag{18}$$

$$c(\mathrm{e}') = c^{\mathrm{b}}(\mathrm{e}')\cdot \mathrm{e}^{\alpha\phi} \tag{19}$$

$$\frac{c(\mathrm{v}_{\mathrm{O}}^{\bullet\bullet})}{c(\mathrm{O}_{\mathrm{O}}^{\times})} = \frac{c^{\mathrm{b}}(\mathrm{v}_{\mathrm{O}}^{\bullet\bullet})}{c^{\mathrm{b}}(\mathrm{O}_{\mathrm{O}}^{\times})}\cdot \mathrm{e}^{-2\alpha\phi} \tag{20}$$

$$\frac{c\left(\mathrm{Acc}_{\mathrm{Ti}}^{'}\right)}{c\left(\mathrm{Acc}_{\mathrm{Ti}}^{\times}\right)} = \frac{c^{\mathrm{b}}\left(\mathrm{Acc}_{\mathrm{Ti}}^{'}\right)}{c^{\mathrm{b}}\left(\mathrm{Acc}_{\mathrm{Ti}}^{\times}\right)}\cdot \mathrm{e}^{\alpha\phi}, \tag{21}$$

with $\alpha := e/(k_{\mathrm{B}}T)$. By combining eqn (14) and (20), one obtains

$$c(\mathrm{v}_{\mathrm{O}}^{\bullet\bullet}) = \frac{\gamma_{\mathrm{O}}c^{\mathrm{b}}(\mathrm{v}_{\mathrm{O}}^{\bullet\bullet})\mathrm{e}^{-2\alpha\phi}}{\gamma_{\mathrm{O}} + c^{\mathrm{b}}(\mathrm{v}_{\mathrm{O}}^{\bullet\bullet})[\mathrm{e}^{-2\alpha\phi} - 1]}. \tag{22}$$

The appropriate terms for the concentrations of $\mathrm{Acc}_{\mathrm{Ti}}^{'}$ and $\mathrm{Acc}_{\mathrm{Ti}}^{\times}$ depend on the considered space-charge scenario. For the Gouy–Chapman (GC) case, eqn (15) and (21) must be combined with the additional condition

$$\frac{c^{\mathrm{GC}}(\mathrm{Acc}_{\mathrm{Ti}}^{'})}{c^{\mathrm{GC}}(\mathrm{Ti}_{\mathrm{Ti}}^{\times})} = \frac{c^{\mathrm{b}}(\mathrm{Acc}_{\mathrm{Ti}}^{'})}{c^{\mathrm{b}}(\mathrm{Ti}_{\mathrm{Ti}}^{\times})}\mathrm{e}^{\alpha\phi}, \tag{23}$$

yielding the expressions

$$c^{\mathrm{GC}}(\mathrm{Acc}_{\mathrm{Ti}}^{'}) = \frac{\gamma_{\mathrm{Ti}}c^{\mathrm{b}}(\mathrm{Acc}_{\mathrm{Ti}}^{'})\mathrm{e}^{\alpha\phi}}{\gamma_{\mathrm{Ti}} + c^{\mathrm{b}}(\mathrm{Acc}_{\mathrm{Ti}}^{'})[\mathrm{e}^{\alpha\phi} - 1]} \tag{24}$$

$$c^{\mathrm{GC}}(\mathrm{Acc}_{\mathrm{Ti}}^{\times}) = \frac{\gamma_{\mathrm{Ti}}c^{\mathrm{b}}(\mathrm{Acc}_{\mathrm{Ti}}^{\times})}{\gamma_{\mathrm{Ti}} + c^{\mathrm{b}}(\mathrm{Acc}_{\mathrm{Ti}}^{'})[\mathrm{e}^{\alpha\phi} - 1]}. \tag{25}$$

In the restricted-equilibrium (RE) case, the overall concentration profile of acceptor cations, $c(\mathrm{Acc}_{\mathrm{Ti}}) \equiv c(\mathrm{Acc}_{\mathrm{Ti}}^{'}) + c(\mathrm{Acc}_{\mathrm{Ti}}^{\times})$, is fixed, keeping the equilibrium profile from $T = T_{\mathrm{crit}}^{\mathrm{cat}}$:

$$c^{\mathrm{RE}}(\mathrm{Acc}_{\mathrm{Ti}}) = c^{\mathrm{crit}}(\mathrm{Acc}_{\mathrm{Ti}}). \tag{26}$$

By combining eqn (26) with eqn (21), one obtains

$$c^{\mathrm{RE}}\left(\mathrm{Acc}_{\mathrm{Ti}}^{'}\right) = \frac{c^{\mathrm{crit}}(\mathrm{Acc}_{\mathrm{Ti}})c^{\mathrm{b}}(\mathrm{Acc}_{\mathrm{Ti}}^{'})\mathrm{e}^{\alpha\phi}}{c^{\mathrm{b}}(\mathrm{Acc}_{\mathrm{Ti}}^{\times}) + c^{\mathrm{b}}(\mathrm{Acc}_{\mathrm{Ti}}^{'})\mathrm{e}^{\alpha\phi}}. \tag{27}$$

Note that eqn (27) may also be applied to the Mott–Schottky[130–132] case, by setting $c^{\mathrm{crit}}(\mathrm{Acc}_{\mathrm{Ti}}) = c^{\mathrm{b}}(\mathrm{Acc}_{\mathrm{Ti}})$.

The grain-boundary core is modelled as an infinitely thin charged plane. The areal charge density in the core, Q^{c}, is taken into account by a Neumann boundary condition:

$$-\varepsilon_{\mathrm{r}}\varepsilon_0(\partial_+\phi(x_{\mathrm{gb}}) - \partial_-\phi(x_{\mathrm{gb}})) = Q^{\mathrm{c}}, \tag{28}$$

where ∂_+ and ∂_- denote the right- and left-hand side derivatives with respect to x, and x_{gb} is the location of the grain boundary. Q^{c} is calculated from formal point-defect concentrations in the core, c^{c}.

$$Q^{\mathrm{c}} = ew^{\mathrm{c}}\cdot\left(2c^{\mathrm{c}}(\mathrm{v}_{\mathrm{O}}^{\bullet\bullet}) + c^{\mathrm{c}}(\mathrm{h}^{\bullet}) - c^{\mathrm{c}}(\mathrm{e}') - c^{\mathrm{c}}(\mathrm{Acc}_{\mathrm{Ti}}^{'})\right). \tag{29}$$

Previous studies have indicated that the structurally distorted region around the grain-boundary plane is several lattice constants wide,[11,133,134] and only some of the sites in it are energetically more favourable than the bulk sites.[118–120] In our model, we attribute a formal width, w^{c}, to the grain-boundary core, and a formal O-site density, $\gamma_{\mathrm{O}}^{\mathrm{c}} < \gamma_{\mathrm{O}}$, such that the areal core-site density is lower than it would be in a bulk slab of the same width.[35] For convenience, we assume that the number of sites in the Ti sublattice as well as the number of electronic interface states is lowered by the same factor, $\gamma_{\mathrm{O}}^{\mathrm{c}}/\gamma_{\mathrm{O}}$. Since, for all defect species except $\mathrm{v}_{\mathrm{O}}^{\bullet\bullet}$, the segregation energy $\Delta\mu^{\ominus}$ is assumed to be zero-valued, the site fractions of these defects are continuous across the grain boundary. That is, we can set

$$\frac{c^{\mathrm{c}}}{\gamma_{\mathrm{O}}^{\mathrm{c}}} = \frac{c(x_{\mathrm{gb}})}{\gamma_{\mathrm{O}}}, \tag{30}$$

while the concentration of $\mathrm{v}_{\mathrm{O}}^{\bullet\bullet}$ in the grain-boundary core is calculated by solving

$$\frac{c^{\mathrm{c}}(\mathrm{v}_{\mathrm{O}}^{\bullet\bullet})}{c^{\mathrm{c}}(\mathrm{O}_{\mathrm{O}}^{\times})} = \frac{c^{\mathrm{b}}(\mathrm{v}_{\mathrm{O}}^{\bullet\bullet})}{c^{\mathrm{b}}(\mathrm{O}_{\mathrm{O}}^{\times})}\cdot \mathrm{e}^{-2\alpha\Phi_0}\cdot \underbrace{\exp\left(-\frac{\Delta\mu_{\mathrm{v}}^{\ominus}}{k_{\mathrm{B}}T}\right)}_{:=f^{\mathrm{c}}},$$

subject to a site-exclusion constraint,

$$c^{\mathrm{c}}(\mathrm{v}_{\mathrm{O}}^{\bullet\bullet}) + c^{\mathrm{c}}(\mathrm{O}_{\mathrm{O}}^{\times}) = \gamma_{\mathrm{O}}^{\mathrm{c}}, \tag{31}$$

which yields

$$c^{\mathrm{c}}(\mathrm{v}_{\mathrm{O}}^{\bullet\bullet}) = \frac{\gamma_{\mathrm{O}}^{\mathrm{c}}c^{\mathrm{b}}(\mathrm{v}_{\mathrm{O}}^{\bullet\bullet})\mathrm{e}^{-2\alpha\Phi_0}\cdot f^{\mathrm{c}}}{\gamma_{\mathrm{O}} + c^{\mathrm{b}}(\mathrm{v}_{\mathrm{O}}^{\bullet\bullet})\cdot[\mathrm{e}^{-2\alpha\Phi_0}\cdot f^{\mathrm{c}} - 1]}. \tag{32}$$

As stated before, this equation assumes implicitly that $\Delta\mu_{\mathrm{v}}^{\ominus}$ varies neither with the number of vacancies present in the core nor with changes in core composition through dopant enrichment. Taking such effects into account comprehensively requires the inclusion, for example, of activity coefficients for defect–defect interactions in the treatment, which then in turn requires numerical values for the activity coefficients to be specified (*e.g.* as a function of defect concentrations and temperature). Since such values are not available, the assumption of a constant $\Delta\mu_{\mathrm{v}}^{\ominus}$ is made out of necessity. And from the point of view of experiment, the assumption is reasonable, since experimental data can be described with a single $\Delta\mu_{\mathrm{v}}^{\ominus}$ value.[35,72] In this sense, $\Delta\mu_{\mathrm{v}}^{\ominus}$ is an effective value in a dilute-solution treatment that to some degree reflects defect–defect interactions.

The model parameters for the simulation of the space-charge layers are summarised in Table 1.

Table 1 Model parameters for the simulation of the space-charge layers

Parameter	Value	Comment
ℓ_{cell}/μm	20	Simulation cell size
x_{gb}/μm	0	Grain-boundary location
c_a^b/cm^{-3}	1.6×10^{19}	Bulk doping level
pO_2/bar	0.2	O_2 partial pressure
γ_O	[Eqn (16)]	Bulk O-site density
γ_{Ti}	[Eqn (16)]	Bulk Ti-site density
a	[Eqn (17)]	Lattice constant
w^c/nm	2	Formal core width
γ_O^c/γ_O	0.05	Core O-site density
$\Delta\mu_v^{\ominus}$/eV	−1.5	$v_O^{\bullet\bullet}$ segregation energy
T_{crit}^{cat}/K	Varied	Negligible cation mobility
T_{crit}^{surf}/K	Varied	Negligible oxygen exchange

3 Results

We simulated grain-boundary space-charge layers in $SrTiO_3$ over a temperature range that encompasses both critical temperatures, that is, T_{crit}^{cat}, the critical temperature above which the acceptor cations achieve electrochemical equilibrium; and T_{crit}^{surf}, the critical temperature above which the chemical equilibrium with the gas phase, eqn (3), is achieved. This leads naturally to the subdivision of the considered temperature range into three regimes: at high temperatures ($T > T_{crit}^{cat}$), the acceptor-cation profiles reach electrochemical equilibrium, and the oxygen sublattice is in chemical equilibrium with oxygen in the gas phase (*full equilibrium*, FE). At intermediate temperatures ($T_{crit}^{surf} < T < T_{crit}^{cat}$), the cation distributions are frozen-in, but chemical equilibrium for oxygen is still attained (*one restricted equilibrium*, 1RE). At low temperatures ($T < T_{crit}^{surf}$), oxygen exchange is also kinetically hindered, and the bulk oxygen-vacancy concentration is frozen-in (*two restricted equilibria*, 2RE).

Exemplary solutions of the Poisson equation [eqn (12)] for the relevant boundary conditions are shown in Fig. 2. The temperatures (T/K = {1400, 800, 300}) were chosen so as

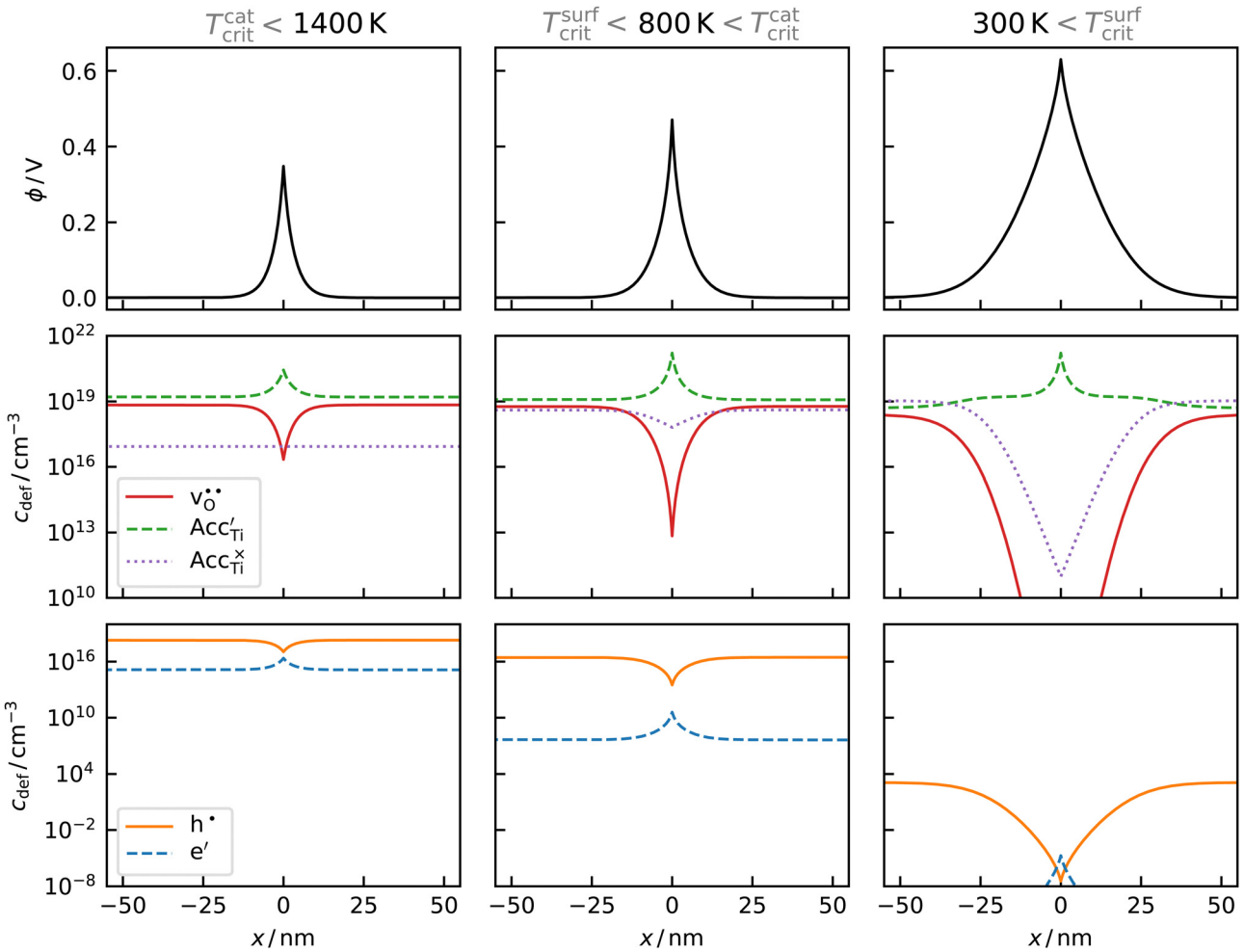

Fig. 2 Simulated grain-boundary space-charge layers in acceptor-doped $SrTiO_3$. Profiles of the electric potential, ϕ, and of the point-defect concentrations, c_{def}, are depicted for three temperatures that represent the three relevant space-charge regimes: full equilibrium (FE) in the range $T_{crit}^{cat} < T$; one restricted-equilibrium (1RE) in the range $T_{crit}^{surf} < T < T_{crit}^{cat}$, and two restricted equilibria (2RE) in the range $T < T_{crit}^{surf}$, with T_{crit}^{cat} = 1000 K and T_{crit}^{surf} = 650 K. Space-charge layer formation is assumed to originate in $v_O^{\bullet\bullet}$ segregation to the grain-boundary core, driven by a difference $\Delta\mu_v^{\ominus}$ = −1.5 eV in the $v_O^{\bullet\bullet}$ standard chemical potential between grain boundary and bulk.

to represent the three different regimes (FE, 1RE, 2RE). Note that the absolute values of Φ_0 depend on the choice of the grain-boundary parameters $\Delta\mu_v^{\ominus}$ and $w^c\gamma_O^c$. The aim of our quantitative analysis is not a precise prediction of these values, but the identification of trends in the $\Phi_0(T)$ behaviour. Visual inspection of the top row indicates that the space-charge potentials at the three different temperatures are not equal, and neither are the space-charge thicknesses: Φ_0 increases with decreasing temperature (0.35 V at 1400 K; 0.47 V at 800 K; 0.63 V at 300 K), and ℓ_{gb} increases ($\approx$20 nm at 1400 K; $\approx$35 nm at 800 K; $\approx$80 nm at 300 K). These results clearly demonstrate that, if Φ_0 and ℓ_{gb} were obtained experimentally for the three different regimes (probably with different methods), and if all possible measurement errors were eliminated, the values obtained for Φ_0 and ℓ_{gb} would differ considerably. We show later that, even though the trend is clear in this case, *i.e.*, Φ_0 and ℓ_{gb} increasing with decreasing T, data extrapolation from one regime to another is non-trivial.

The second row of Fig. 2 shows the behaviour of the ionic defects within the space-charge layers. One perceives that the behaviour of the acceptor cations changes once the acceptor distribution is frozen-in at T_{crit}^{cat}. While the neutral acceptors, $Acc_{Ti}^{\times}$, may be neglected in the FE case and exhibit an essentially uniform concentration profile, they are depleted in the RE regimes (weakly at T = 800 K and extremely strongly at T = 300 K in Fig. 2), even though they are effectively neutral. This depletion occurs because of the shift of the ionisation equilibrium, eqn (5). The concentration profile of $Acc_{Ti}^{'}$, in turn, develops a plateau region in the outer parts of the space-charge layer, which is clearly visible at 300 K.

The concentration profiles of the electronic defects $h^{\bullet}$ and e' are shown in the bottom row of Fig. 2. These profiles indicate that the bulk concentrations of electronic defects fall drastically with decreasing temperature: between 1400 K and 300 K, $c^b(h^{\bullet})$ decreases by 15 orders of magnitude, and $c^b(e')$ decreases by 30 orders of magnitude. With $c^b(h^{\bullet}) = 1 \times 10^3$ cm^{-3} and $c^b(e') = 5 \times 10^{-16}$ cm^{-3}, the material may be considered free of electronic defects at 300 K. Already at 800 K, however, the electronic defects do not contribute substantially to the charge density in the space-charge layer; compared to $c(Acc_{Ti}^{'})$, $c(h^{\bullet})$ is lower by more than a factor 400, and $c(e')$ by more than 11 orders of magnitude, throughout the space-charge layer.

3.1 The dependence of Φ_0 on temperature and on thermal history

In order to demonstrate the problem of unifying data between the different regimes, we show in Fig. 3 the variation in Φ_0 across a temperature range that includes both T_{crit}^{cat} and T_{crit}^{surf}. Different thermal histories of a sample were modelled by varying both T_{crit}^{cat} and T_{crit}^{surf}. To illustrate the influence of the freezing-in processes, we also calculated the temperature-dependent behaviour without the two processes being frozen-in (as indicated by the dashed and dotted lines, respectively). In Fig. 3, one sees, starting from high temperatures in the FE regime, that Φ_0 increases weakly with decreasing temperature.

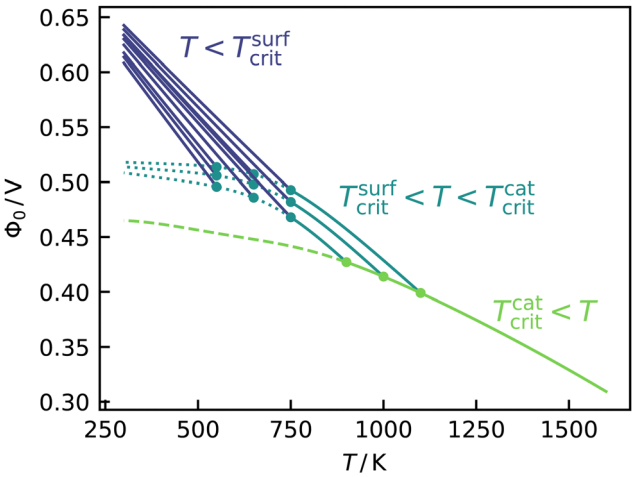

Fig. 3 Simulated space-charge potentials, Φ_0, as a function of temperature, given different thermal histories, which are represented by a variation of T_{crit}^{cat} and T_{crit}^{surf}, with T_{crit}^{cat}/K = {900, 1000, 1100} and T_{crit}^{surf}/K = {550, 650, 750}.

If the sample now experiences the freezing-in of the acceptor-cation profiles at T_{crit}^{cat}/K = 1100, 1000 or 900, Φ_0 increases sharply. There is a clear difference between the actual behaviour with the frozen-in Acc_{Ti} profile (1RE) and the behaviour that would be obtained if the FE regime could be extended down to lower temperatures. In Fig. 3, one also sees, upon further cooling down of the sample through T_{crit}^{surf}/K = 750, 650 or 550, another sharp increase in Φ_0. And similarly, there is a difference between the actual behaviour with frozen-in oxygen-vacancy concentration (2RE) and the behaviour that would result if the sample could still equilibrate with the gas phase (for more detailed explanations, see ESI,† Fig. S1). The abrupt changes in the $\Phi_0(T)$ curve's behaviour, both at T_{crit}^{cat} and T_{crit}^{surf}, reflect the simplified model of the processes being abruptly frozen-in. In reality, the transitions between the different regimes must be expected to take place more smoothly, possibly with hysteresis (arising from whether the sample is heated or cooled).

It is evident in Fig. 3 that values of Φ_0 gathered in different temperature ranges (FE, 1RE, 2RE) will generally differ from one another (see also ESI,† Fig. S2). In the case of T_{crit}^{cat} = 1100 K and T_{crit}^{surf} = 550 K, for instance, electrical measurements carried out in the range of, say, 600 < T/K < 800 would probe values of Φ_0 between 0.48 V and 0.51 V, whereas room-temperature imaging techniques would probe a value of 0.62 V. This may seem a small difference, but constructing a detailed, quantitative model requires a more precise set of data for $\Phi_0(T)$ than Φ_0 is (0.5 to 0.6) V. The most problematic aspect about the differences, however, is not their magnitude—it is the non-trivial behavior as a function of temperature. If only data for the 1RE regime for 600 < T/K < 800 were available, it would appear that Φ_0 approached a plateau, and one would be inclined to take this plateau value, of $\approx$0.51 V, for all temperatures down to room temperature (Φ_0 does not vary linearly with temperature, so that a linear extrapolation would be inappropriate). This value is, however, substantially lower than

the actual (2RE) value of 0.62 V. This difference may also seem small, but macroscopic grain-boundary parameters, such as the grain-boundary resistance, depend exponentially on $\alpha\Phi_0$, so the changing behaviour of $\Phi_0(T)$ at a critical temperature implies a non-trivial temperature dependence also of these observables. In fact, if the grain-boundary resistance at a low temperature (below T_{crit}^{surf}) should, for instance, be predicted by extrapolating a set of electrical resistances obtained at temperatures $> T_{crit}^{surf}$, the extrapolated values would deviate strongly from the true ones. This illustrates how the non-trivial $\Phi_0(T)$ behaviour can cause severe errors even when a value of Φ_0 is not extracted at all from the experimental data. The different temperature ranges, and in particular, the kinetic hindrance of cation migration and oxygen surface exchange must be taken into account in order to achieve a consistent description of grain-boundary properties.

It has been pointed out before that results obtained for a single grain boundary will not generally be representative of a sample's grain-boundary population.[36,37,63] Based on the considerations above, we extend this statement: such results will be quantitatively reproduceable, for the given grain-boundary type, only if the measurements are interpreted in conjunction with the sample's thermal history. Two microstructurally identical samples would exhibit, at the same temperature, different grain-boundary properties if they had previously been subjected to different thermal histories. If, for instance, one sample was cooled down slowly after sintering and the other was quenched quickly, the cation profiles at the grain boundaries within these two samples will correspond to T_{crit}^{cat} values well below and close to the sintering temperature, respectively. The variation of thermal histories is not merely a matter of different sample preparation routes, however. Even if, within a single ceramic sample, all grain boundaries showed identical behaviour in the FE regime (and this is unlikely for $SrTiO_3$[36,37]), the grain boundaries would show different behaviour in the 1RE regime on account of having different T_{crit}^{cat}, arising from the sample's outer regions cooling more rapidly than its centre.

The considerations above illustrate that choosing appropriate values of T_{crit}^{cat} and T_{crit}^{surf} is not a simple task, and as a result, the uncertainty in T_{crit}^{cat} and T_{crit}^{surf} will generally propagate to an uncertainty in Φ_0, as indicated, *e.g.*, by the variation in Φ_0 at 300 K in Fig. 3. Compared to the deviations that would result from disregarding the freezing-in of the processes, however, this variation is relatively small: specifically, for the different (T_{crit}^{cat}, T_{crit}^{surf}) combinations, differences in Φ_0 of about $\pm 2.5\%$ are obtained, whereas Φ_0 is predicted to be $\sim 20\%$ lower in the scope of the 1RE regime, and $\sim 25\%$ lower in the scope of the FE regime. That is, although only rough estimates of these critical temperatures will typically be available, the accuracy of the space-charge model can still be improved considerably by taking the two restricted equilibria into account.

3.2 Comparing different measures of the space-charge layer width

Like Φ_0, the space-charge layer width ℓ_{gb} is also temperature-dependent (see Fig. 2), so values obtained in different temperature ranges are not directly comparable. In the case of ℓ_{gb}, however, there is an additional problem: it is not a uniquely defined quantity.[135] Rather, there are various measures of a grain-boundary's thickness. Let us first set aside the grain boundary's *structural* width, which represents the extent of the region of disrupted lattice periodicity.[136,137] It is typically obtained from electron micrographs, and values are of the order of a few lattice constants.[11,133,134] In a space-charge picture, it may be identified with the width of the grain-boundary core. In terms of space-charge widths, there are three possibilities. The first two, the *electrical* width[138,139] and the *diffusional* width,[135,140] correspond to the regions over which transport properties are altered by the space-charge layers. Specifically, the electrical width probes the extent of the charge-carrier hindrance across a grain boundary and is typically obtained from capacitance data (C_{gb}/C_b) of an impedance spectroscopy measurement; in contrast, the diffusional width probes the extent of enhanced transport along a grain boundary, and its determination is not trivial.[135] The third possibility, the *chemical* width,[136–138] is itself not a uniquely defined property. Instead, a chemical width can be attributed, in principle, to every chemical species in the system, by taking the width of the grain-boundary feature in the respective concentration profile. It can be determined, for example, from the dopant concentration profiles measured by EELS or APT. Reported chemical widths are typically of the order of several nanometers.[65–67,141] Electrical widths, on the other hand, show a strong variation; in acceptor-doped $SrTiO_3$, thicknesses have been reported in the range of tens to hundreds of nanometers.[7,8,14,33]

To study the differences between chemical and electrical widths in more detail, we extracted both quantities from a set of simulated space-charge configurations at T/K = {500, 700, 1000}. A chemical width of ~ 20 nm was estimated by visual inspection of the Acc_{Ti} concentration profile (see Fig. 4a). Although the concentration profiles of Acc'_{Ti} and $Acc^{\times}_{Ti}$ depend on the temperature, this value remains unchanged, since $c(Acc_{Ti})$ is frozen-in below T_{crit}^{cat} = 1000 K. The electrical grain-boundary width is typically obtained from C_{gb}/C_b. In a previous study,[73] we found that, for a dilute solution of charge carriers, the electrical width can be estimated‡ from the inflection points of the local conductivity profile, $\sigma_{loc}(x)$ (see Fig. 4b). This was calculated as $\sigma_{loc} = e \cdot [2u_v c(v_O^{\bullet\bullet}) + u_h c(h^{\bullet}) + u_e c(e')]$, with the electrical mobilities (u_v, u_h, u_e) taken from ref. 79. The electrical width obtained in this way increases from 11 nm at T = 1000 K to 27 nm at T = 700 K, and further to 46 nm upon cooling to T = 500 K. Consistent with the above-mentioned differences between experimentally measured chemical and electrical widths, we find that the chemical width underestimates the extent of the space-charge layer for $T < T_{crit}^{cat}$, most severely (by a factor >2) at the lowest temperature. Note that the results presented here presuppose that electrochemical

‡ On occasion, impedance spectra are calculated directly from $c_{def}(x)$ or $\phi(x)$ profiles in the literature, by applying the Maxwell–Wagner approximation. This is not a suitable approximation for space-charge layers, however.[142] Impedance spectra can only be obtained from such profiles by means of drift–diffusion simulations; either explicitly time-dependent[73] or linearised, in Fourier space.[142]

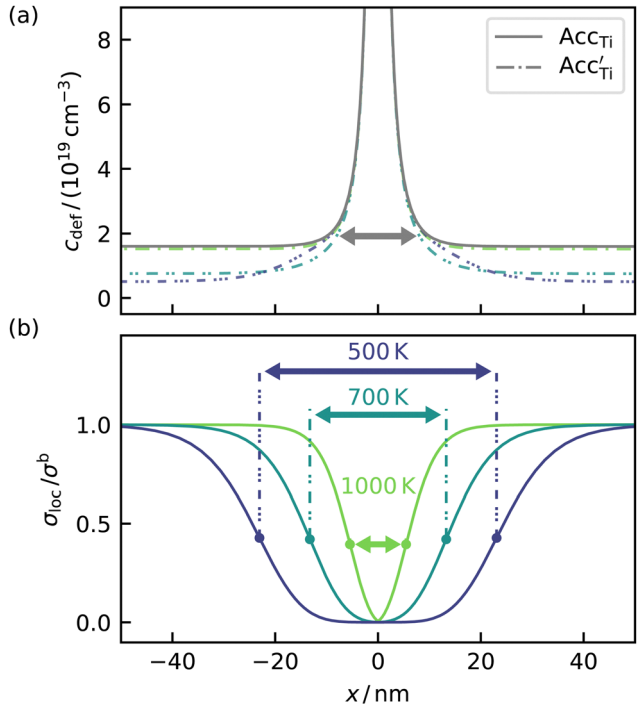

Fig. 4 Illustration of the discrepancies between different measures of the space-charge width for exemplary restricted-equilibrium space-charge layers at T/K = {500, 700, 1000}, with T_{crit}^{cat} = 1000 K and T_{crit}^{surf} = 650 K: (a) a chemical width is estimated from the concentration profiles of Acc_{Ti}, Acc'_{Ti} profiles are shown for comparison; (b) the electrical width is estimated from local-conductivity profiles, σ_{loc}, calculated from the concentration profiles as $e \cdot \left[2u_v c(v_O^{\bullet\bullet}) + u_h c(h^{\bullet}) + u_e c(e')\right]$.

equilibrium of the acceptor-cation profile is actually established at T_{crit}^{cat}. In reality, this may not always be the case, especially if an accelerated sintering method (such as spark plasma sintering[143,144] or flash sintering[145]) is applied,[84,146,147] and it is reasonable to assume that the discrepancies between chemical and electrical width can be even larger in such cases.

The substantial difference between the chemical and electrical widths is indicative of a fundamental disparity in the information that they convey. Typically, both quantities will be obtained at a temperature well below T_{crit}^{cat}, and hence, the Acc_{Ti} profile will then be frozen-in. As a consequence, the chemical width of the Acc_{Ti} profile reflects the state of the space-charge layer at T_{crit}^{cat}, rather than its state at the measurement temperature T.§ The electrical width, in turn, probes primarily the width of the $h^{\bullet}/v_O^{\bullet\bullet}$ depletion layer, which is assumed reasonably to reach electrochemical equilibrium.

4 Discussion

When determining and comparing data from different experimental methods, conflicting data may demand that the results be prioritised by their levels of reliability. For the extraction of Φ_0 and ℓ_{gb}, one may be inclined to trust imaging results more than electrical measurements, since they do not require a preconceived space-charge model (*e.g.*, Gouy–Chapman or Mott–Schottky). Since such results are generally obtained for a single grain boundary, however, they will not be representative of the variety of grain-boundary types and their different properties within a ceramic's grain-boundary population,[15,63] and the same goes for electrical measurements on a specific bicrystal. Electrical measurements on ceramic samples, in contrast, do probe the grain-boundary population representatively, but at the cost of losing microscopic information:[70] the arcs in impedance spectra, for instance, are typically associated with the microscopic electrical properties in the scope of the *brick-layer* model[139] for the microstructure. This simplification has been demonstrated to yield good estimates of microscopic properties, provided that the grain-size distribution is monomodal and not too wide.[8,14,68,69,148,149] Φ_0 is typically extracted from electrical data by closed-form expressions that neglect defect interactions and that require the interfacial defect chemistry to conform to a Mott–Schottky model. In concentrated solutions, such expressions have been shown to be unsuitable.[85,150] In dilute solutions, however, Φ_0 may be extracted with an error of only a few percent.[73] The validity of the employed space-charge model can be put to a test with different consistency checks.[71,73] By applying these formulas to electrical data obtained for acceptor-doped $SrTiO_3$, plausible values of Φ_0 have consistently been obtained in the literature.[12,14,35,37,41]

Imaging techniques, in contrast, have not yet succeeded at providing plausible estimates of Φ_0 in acceptor-doped $SrTiO_3$. The electrostatic grain-boundary barriers observed by SPM are unreasonably low (several tens of mV) in view of their being up to a few micrometers wide.[64] Elemental profiles from EELS have only been reported for the acceptor dopants, and, while the observed accumulation of Acc_{Ti} at the grain boundaries[11,65–67] is consistent with the presence of depletion layers, Φ_0 was not obtained from this (and if it was, it would refer to the state of the system at T_{crit}^{cat}, rather than at the measurement temperature, as discussed in the previous section). The results of a recent DPC study[62] are also consistent with the presence of depletion layers, but Φ_0 could not be extracted quantitatively. Lastly, electron holography yields a highly incoherent picture: the reported phase shifts at the grain boundaries are typically negative,[67,75,76,151] although positive phase shifts have also been reported.[74,152] Not only does this oppose the extensive evidence in favour of a depletion-layer model for acceptor-doped samples, but the calculated space-charge potentials are also unphysically large (~ -4 V) in some cases:[67,151] for a semiconductor, such as $SrTiO_3$, with a bandgap of 3 eV, Φ_0 is constrained to lie between $\sim +3$ V and ~ -3 V,[35] and these upper and lower bounds can only be reached if the Fermi level in the bulk is at the edge of the valence or conduction band, respectively.

These inaccuracies indicate that the mentioned imaging techniques are prone to disturbing influences. In SPM, the potential is measured at a distance from the surface, and hence, surface roughness and unknown surface charges can make a reconstruction of potential differences within the

§ The equilibrium width of the space-charge layer could be probed, in principle, if valence-state-sensitive measurements of the Acc'_{Ti} and $Acc^{\times}_{Ti}$ concentration profiles could be achieved with a very high precision and sensitivity.

sample difficult, if not impossible.[35,64] With regard to DPC, in turn, it has been argued that quantitative measurements could only be achieved if the TEM specimen was scaled down to nanometer dimensions, at which the space-charge layer properties would be compromised by finite-size effects.[62] The severe inconsistencies in electron-holographic measurements point towards a conceptual problem: beside the space-charge potential, also topographic, structural and chemical changes in the grain-boundary region are reflected in the electron phase shift. If these influences cannot be neglected, the phase shift at the grain boundary will not be a measure of Φ_0.[67,74–77]

Given pristine grain boundaries in dilute solid solutions, electrical measurements are currently the most reliable way to assess the space-charge potential, Φ_0. In the development and refinement of imaging techniques for the analysis of space-charge properties, the accuracy of a measurement should, therefore, be appraised by comparing it with electrical measurements.

A joining of imaging techniques and electrical methods can also be highly useful in identifying the relationships between grain-boundary structure, composition, and conductivity. It has been demonstrated recently that a thorough treatment of imaging data can help bridge the gap between microscopic observations and macroscopic conductivity.[63] Further investigations on the microscopic structure–composition–conductivity relations are a promising route in making ceramic conductivities more predictable. Unless both electrical and imaging measurements are carried out under the same conditions (*e.g.*, by appropriate *in situ* approaches), such endeavours will generally face the issue of unifying data from different temperature ranges.

A direct comparison of elevated-temperature electrical data with room-temperature data from imaging techniques implicitly presupposes that one specific value can be attributed to Φ_0 and/or ℓ_{gb} for a given material. Neither Φ_0 nor ℓ_{gb}, however, are material-specific properties. They depend, of course, on material-specific parameters, but also on the thermodynamic conditions (T, pO_2), on the grain-boundary type,[36,37,63] and on the sample's thermal history.

5 Conclusions

We simulated grain-boundary space-charge layers in $SrTiO_3$ at different temperatures, with a focus on the characteristic temperature ranges of electrical methods, on the one hand, and imaging techniques, on the other hand. Various thermal histories were represented by varying the critical temperatures of cation redistribution, T_{crit}^{cat}, and of the oxygen surface exchange, T_{crit}^{surf}.

We treated the trends in $\Phi_0(T)$ as a proxy for grain-boundary properties as a function of temperature. In the case considered, we found that Φ_0 generally increased with decreasing temperature, but at the onset of a restricted equilibrium, at T_{crit}^{cat} and then at T_{crit}^{surf}, the increase became substantially more pronounced. From our results, we identified some general problems that may arise when data gathered by different experimental approaches are considered together.

1. An extrapolation of grain-boundary properties across the transitions between restricted equilibria (*e.g.*, from electrical measurement conditions to room temperature) will lead to large errors.

2. The critical temperatures can be difficult to estimate. Even when only a very rough estimate can be made, however, taking the frozen processes into account will strongly enhance the accuracy of a space-charge model.

3. When the acceptor-cation redistribution is frozen-in, the chemical width from acceptor-cation profiles will underestimate the space-charge layer's thickness. The electrical grain-boundary width from impedance spectroscopy is a more reliable measure of its full extent.

In summary, our results demonstrate that probing the behaviour of grain-boundary space-charge layers in electroceramics in different temperature ranges will naturally yield values of characteristic parameters that are different and not trivially related. Owing to these non-trivial differences, the grain-boundary properties of an electroceramic oxide as a function of temperature may be understood and predicted only within the scope of a space-charge model that takes into account both restricted equilibria.

Author contributions

Adrian L. Usler: methodology, software, investigation, writing – original draft, visualisation, writing – review & editing. Fabian Ketter: investigation, writing – review & editing, visualisation. Roger A. De Souza: conceptualization, supervision, writing – original draft, writing – review & editing, project administration, funding acquisition.

Conflicts of interest

There are no conflicts to declare.

Acknowledgements

This work was supported by RWTH Aachen University and by the Deutsche Forschungsgemeinschaft (DFG, German Research Foundation) within the Priority Programme (SPP1959) ''Fields-Matter'' under project DE 2854/9-2 and within the Sonderforschungsbereich (collaborative research centre) SFB 1548, FLAIR (Fermi Level Engineering applied to oxide electroceramics).

Notes and references

1 R. A. De Souza, J. Fleig, R. Merkle and J. Maier, *Int. J. Mater. Res.*, 2022, **94**, 218–225.
2 D. Singh, M. Lorenzo-Martin, G. Chen, F. Gutiérrez-Mora and J. L. Routbort, *J. Eur. Ceram. Soc.*, 2007, **27**, 3377–3384.
3 L. Porz, M. Scherer, M. Höfling, A. Nakamura, W. Rheinheimer and J. Rödel, *J. Mater. Sci.*, 2023, **58**, 2430–2438.

4 E. R. Pfeiffer and J. F. Schooley, *Phys. Lett. A*, 1969, **29**, 589–590.
5 H. Suzuki, H. Kurosawa, J. Chen, Y. Hirotsu, K. Nakajima, T. Yamashita, H. Myoren and Y. Osaka, *Supercond. Sci. Technol.*, 1991, **4**, 479.
6 T. R. N. Kutty and S. Philip, *Mater. Sci. Eng., B*, 1995, **33**, 58–66.
7 I. Denk, J. Claus and J. Maier, *J. Electrochem. Soc.*, 1997, **144**, 3526.
8 S. Rodewald, J. Fleig and J. Maier, *J. Am. Ceram. Soc.*, 2001, **84**, 521–530.
9 D.-H. Kwon, S. Lee, C. S. Kang, Y. S. Choi, S. J. Kang, H. L. Cho, W. Sohn, J. Jo, S.-Y. Lee, K. H. Oh, T. W. Noh, R. A. De Souza, M. Martin and M. Kim, *Adv. Mater.*, 2019, **31**, 1901322.
10 J. Maier, G. Schwitzgebel and H.-J. Hagemann, *J. Solid State Chem.*, 1985, **58**, 1–13.
11 F. Noll, W. Münch, I. Denk and J. Maier, *Solid State Ion.*, 1996, **86**, 711–717.
12 M. Vollmann, R. Hagenbeck and R. Waser, *J. Am. Ceram. Soc.*, 1997, **80**, 2301–2314.
13 J. R. Jurado, M. T. Colomer and J. R. Frade, *J. Am. Ceram. Soc.*, 2000, **83**, 2715–2720.
14 J. Fleig, S. Rodewald and J. Maier, *J. Appl. Phys.*, 2000, **87**, 2372–2381.
15 R. A. De Souza, J. Fleig, J. Maier, O. Kienzle, Z. Zhang, W. Sigle and M. Rühle, *J. Am. Ceram. Soc.*, 2003, **86**, 922–928.
16 R. Meyer and R. A. De Souza, *Electrochemical Society Proceedings*, 2003, p. 220.
17 D. W. Wang and A. S. Nowick, *J. Solid State Chem.*, 1980, **35**, 325–333.
18 R. Gerhardt and A. S. Nowick, *J. Am. Ceram. Soc.*, 1986, **69**, 641–646.
19 X. Guo and R. Waser, *Prog. Mater. Sci.*, 2006, **51**, 151–210.
20 H. J. Avila-Paredes and S. Kim, *Solid State Ion.*, 2006, **177**, 3075–3080.
21 J. Bauerle, *J. Phys. Chem. Solids*, 1969, **30**, 2657–2670.
22 T. Van Dijk and A. J. Burggraaf, *Phys. Status Solidi A*, 1981, **63**, 229–240.
23 M. J. Verkerk, B. J. Middelhuis and A. J. Burggraaf, *Solid State Ion.*, 1982, **6**, 159–170.
24 K. Huang, R. S. Tichy and J. B. Goodenough, *J. Am. Ceram. Soc.*, 1998, **81**, 2576–2580.
25 H. J. Park and S. Kim, *J. Phys. Chem. C*, 2007, **111**, 14903–14910.
26 K. D. Kreuer, *Solid State Ion.*, 1999, **125**, 285–302.
27 H. G. Bohn and T. Schober, *J. Am. Ceram. Soc.*, 2000, **83**, 768–772.
28 F. Iguchi, N. Sata, T. Tsurui and H. Yugami, *Solid State Ion.*, 2007, **178**, 691–695.
29 P. Babilo, T. Uda and S. M. Haile, *J. Mater. Res.*, 2007, **22**, 1322–1330.
30 S. Tao and J. T. S. Irvine, *J. Solid State Chem.*, 2007, **180**, 3493–3503.
31 S. M. Haile, D. L. West and J. Campbell, *J. Mater. Res.*, 1998, **13**, 1576–1595.
32 W. G. Coors and D. W. Readey, *J. Am. Ceram. Soc.*, 2002, **85**, 2637–2640.
33 M. Vollmann and R. Waser, *J. Am. Ceram. Soc.*, 1994, **77**, 235–243.
34 R. Hagenbeck and R. Waser, *J. Appl. Phys.*, 1998, **83**, 2083–2092.
35 R. A. De Souza, *Phys. Chem. Chem. Phys.*, 2009, **11**, 9939–9969.
36 R. A. De Souza, J. Fleig, J. Maier, Z. Zhang, W. Sigle and M. Rühle, *J. Appl. Phys.*, 2005, **97**, 053502.
37 Z. Zhang, W. Sigle, R. A. De Souza, W. Kurtz, J. Maier and M. Rühle, *Acta Mater.*, 2005, **53**, 5007–5015.
38 P. Balaya, M. Ahrens, L. Kienle, J. Maier, B. Rahmati, S. B. Lee, W. Sigle, A. Pashkin, C. Kuntscher and M. Dressel, *J. Am. Ceram. Soc.*, 2006, **89**, 2804–2811.
39 I. Denk, F. Noll and J. Maier, *J. Am. Ceram. Soc.*, 1997, **80**, 279–285.
40 M. Leonhardt, J. Jamnik and J. Maier, *Electrochem. Solid-State Lett.*, 1999, **2**, 333.
41 X. Guo, J. Fleig and J. Maier, *J. Electrochem. Soc.*, 2001, **148**, J50.
42 X. Guo, J. Fleig and J. Maier, *Solid State Ion.*, 2002, **154**, 563–569.
43 P. Balaya, J. Jamnik, J. Fleig and J. Maier, *Appl. Phys. Lett.*, 2006, **88**, 062109.
44 P. Balaya, J. Jamnik, J. Fleig and J. Maier, *J. Electrochem. Soc.*, 2007, **154**, P69.
45 G. Gregori, P. Lupetin and J. Maier, *ECS Trans.*, 2012, **45**, 19.
46 Y. Wu, P. C. Bowes, J. N. Baker and D. L. Irving, *J. Appl. Phys.*, 2020, **128**, 014101.
47 T. Hölbling and R. Waser, *J. Appl. Phys.*, 2002, **91**, 3037–3043.
48 S. K. Kim, S. Khodorov, C.-T. Chen, S. Kim and I. Lubomirsky, *Phys. Chem. Chem. Phys.*, 2013, **15**, 8716–8721.
49 S. K. Kim, S. Khodorov, I. Lubomirsky and S. Kim, *Phys. Chem. Chem. Phys.*, 2014, **16**, 14961–14968.
50 S. Kim, S. K. Kim, S. Khodorov, J. Maier and I. Lubomirsky, *Phys. Chem. Chem. Phys.*, 2016, **18**, 3023–3031.
51 J. M. R. Weaver and H. K. Wickramasinghe, *J. Vac. Sci. Technol., B: Nanotechnol. Microelectron.: Mater., Process., Meas., Phenom.*, 1991, **9**, 1562–1565.
52 W. Nabhan, B. Equer, A. Broniatowski and G. De Rosny, *Rev. Sci. Instrum.*, 1997, **68**, 3108–3111.
53 D. R. Diercks, J. Tong, H. Zhu, R. Kee, G. Baure, J. C. Nino, R. O'Hayre and B. P. Gorman, *J. Mater. Chem. A*, 2016, **4**, 5167–5175.
54 B. Gault, A. Chiaramonti, O. Cojocaru-Mirédin, P. Stender, R. Dubosq, C. Freysoldt, S. K. Makineni, T. Li, M. Moody and J. M. Cairney, *Nat. Rev. Methods Primers*, 2021, **1**, 51.
55 D. R. Clark, D. R. Diercks, S. Ricote, T. T. Dearden, N. P. Sullivan, J. W. Medlin, B. P. Gorman and R. P. OHayre, *J. Mater. Chem. C*, 2023, **11**, 5082–5091.
56 P. G. Merli, G. F. Missiroli and G. Pozzi, *Phys. Status Solidi A*, 1975, **30**, 699–711.
57 S. Frabboni, G. Matteucci, G. Pozzi and M. Vanzi, *Phys. Rev. Lett.*, 1985, **55**, 2196.

58 W.-D. Rau, P. Schwander and A. Ourmazd, *Solid State Phenom.*, 1998, **63**, 525–528.
59 W.-D. Rau, P. Schwander, F. H. Baumann, W. Höppner and A. Ourmazd, *Phys. Rev. Lett.*, 1999, **82**, 2614.
60 N. Shibata, S. D. Findlay, Y. Kohno, H. Sawada, Y. Kondo and Y. Ikuhara, *Nat. Phys.*, 2012, **8**, 611–615.
61 K. Müller-Caspary, T. Grieb, J. Müßener, N. Gauquelin, P. Hille, J. Schörmann, J. Verbeeck, S. Van Aert, M. Eickhoff and A. Rosenauer, *Phys. Rev. Lett.*, 2019, **122**, 106102.
62 C. Yang, Y. Wang, W. Sigle and P. A. van Aken, *Nano Lett.*, 2021, **21**, 9138–9145.
63 W. J. Bowman, A. Darbal and P. A. Crozier, *ACS Appl. Mater. Interfaces*, 2019, **12**, 507–517.
64 B. D. Huey and D. A. Bonnell, *Solid State Ion.*, 2000, **131**, 51–60.
65 Y.-M. Chiang and T. Takagi, *J. Am. Ceram. Soc.*, 1990, **73**, 3278–3285.
66 N. Wilcox, V. Ravikumar, R. Rodrigues, V. Dravid, M. Vollmann, R. Waser, K. Soni and A. Adriaens, *Solid State Ion.*, 1995, **75**, 127–136.
67 S. J. P. Longworth, K. M. Knowles and R. E. Dunin-Borkowski, *J. Phys.: Conf. Ser.*, 2006, 235.
68 J. Fleig and J. Maier, *J. Electrochem. Soc.*, 1998, **145**, 2081.
69 J. Fleig and J. Maier, *J. Eur. Ceram. Soc.*, 1999, **19**, 693–696.
70 J. Fleig, *Solid State Ion.*, 2000, **131**, 117–127.
71 S. Kim, *Phys. Chem. Chem. Phys.*, 2016, **18**, 19787–19791.
72 J. P. Parras, C. Cao, Z. Ma, R. Mücke, L. Jin, R. Dunin-Borkowski, O. Guillon and R. A. De Souza, *J. Am. Ceram. Soc.*, 2020, **103**, 1755–1764.
73 A. L. Usler and R. A. De Souza, *J. Electrochem. Soc.*, 2021, **168**, 056504.
74 H. R. Liu, Y. G. Wang, Q. X. Liu and Q. B. Yang, *J. Phys. D: Appl. Phys.*, 2004, **37**, 1478.
75 C. T. Koch, *Int. J. Mater. Res.*, 2010, **101**, 43–49.
76 S. von Alfthan, N. A. Benedek, L. Chen, A. Chua, D. Cockayne, K. J. Dudeck, C. Elsässer, M. W. Finnis, C. T. Koch and B. Rahmati, *et al.*, *Annu. Rev. Mater. Res.*, 2010, **40**, 557–599.
77 T. Bondevik, H. H. Ness, C. Bazioti, T. Norby, O. M. Løvvik, C. T. Koch and Ø. Prytz, *Phys. Chem. Chem. Phys.*, 2019, **21**, 17662–17672.
78 R. Waser, *J. Am. Ceram. Soc.*, 1991, **74**, 1934–1940.
79 I. Denk, W. Münch and J. Maier, *J. Am. Ceram. Soc.*, 1995, **78**, 3265–3272.
80 R. A. De Souza and A. H. H. Ramadan, *Phys. Chem. Chem. Phys.*, 2013, **15**, 4505–4509.
81 R. A. Maier and C. A. Randall, *J. Am. Ceram. Soc.*, 2016, **99**, 3350–3359.
82 J.-S. Lee and D.-Y. Kim, *J. Mater. Res.*, 2001, **16**, 2739–2751.
83 A. Tschöpe, S. Kilassonia and R. Birringer, *Solid State Ion.*, 2004, **173**, 57–61.
84 M. Shirpour, B. Rahmati, W. Sigle, P. A. van Aken, R. Merkle and J. Maier, *J. Phys. Chem. C*, 2012, **116**, 2453–2461.
85 X. Tong, D. S. Mebane and R. A. De Souza, *J. Am. Ceram. Soc.*, 2020, **103**, 5–22.
86 T. Scherban, W. K. Lee and A. S. Nowick, *Solid State Ion.*, 1988, **28**, 585–588.
87 J. F. Liu and A. S. Nowick, *Solid State Ion.*, 1992, **50**, 131–138.
88 J. Maier, *Solid State Ion.*, 1996, **86**, 55–67.
89 J. Müller, K. D. Kreuer, J. Maier, S. Matsuo and M. Ishigame, *Solid State Ion.*, 1997, **97**, 421–427.
90 H. G. Bohn, T. Schober, T. Mono and W. Schilling, *Solid State Ion.*, 1999, **117**, 219–228.
91 K. Sasaki, J. Claus and J. Maier, *Solid State Ionics*, 1999, **121**, 51–60.
92 K. Sasaki and J. Maier, *J. Eur. Ceram. Soc.*, 1999, **19**, 741–745.
93 E. Bucher, A. Egger, P. Ried, W. Sitte and P. Holtappels, *Solid State Ionics*, 2008, **179**, 1032–1035.
94 R. Zohourian, R. Merkle, G. Raimondi and J. Maier, *Adv. Funct. Mater.*, 2018, **28**, 1801241.
95 K. Gömann, G. Borchardt, M. Schulz, A. Gömann, W. Maus-Friedrichs, B. Lesage, O. Kaïtasov, S. Hoffmann-Eifert and T. Schneller, *Phys. Chem. Chem. Phys.*, 2005, **7**, 2053–2060.
96 A. R. Genreith-Schriever and R. A. De Souza, *Phys. Rev. B*, 2016, **94**, 224304.
97 D. Kemp and R. A. De Souza, *Phys. Rev. Mater.*, 2021, **5**, 105401.
98 P. Virtanen, R. Gommers, T. E. Oliphant, M. Haberland, T. Reddy, D. Cournapeau, E. Burovski, P. Peterson, W. Weckesser, J. Bright, S. J. van der Walt, M. Brett, J. Wilson, K. J. Millman, N. Mayorov, A. R. J. Nelson, E. Jones, R. Kern, E. Larson, C. J. Carey, I. Polat, Y. Feng, E. W. Moore, J. VanderPlas, D. Laxalde, J. Perktold, R. Cimrman, I. Henriksen, E. A. Quintero, C. R. Harris, A. M. Archibald, A. H. Ribeiro, F. Pedregosa, P. van Mulbregt and SciPy 1.0 Contributors, *Nat. Methods*, 2020, **17**, 261–272.
99 R. C. Kirby and A. Logg, *ACM Trans. Math. Softw*, 2006, **32**(3), 417–444.
100 A. Logg and G. N. Wells, *ACM Trans. Math. Softw*, 2010, **37**(2), 20.
101 A. Logg, K.-A. Mardal and G. Wells, *Automated solution of differential equations by the finite element method: The FEniCS book*, Springer Science & Business Media, 2012, vol. 84.
102 M. S. Alnæs, A. Logg, K. B. Ølgaard, M. E. Rognes and G. N. Wells, *ACM Trans. Math. Softw.*, 2014, **40**, 1–37.
103 C. R. Harris, K. J. Millman, S. J. van der Walt, R. Gommers, P. Virtanen, D. Cournapeau, E. Wieser, J. Taylor, S. Berg, N. J. Smith, R. Kern, M. Picus, S. Hoyer, M. H. van Kerkwijk, M. Brett, A. Haldane, J. Fernández del Río, M. Wiebe, P. Peterson, P. Gérard-Marchant, K. Sheppard, T. Reddy, W. Weckesser, H. Abbasi, C. Gohlke and T. E. Oliphant, *Nature*, 2020, **585**, 357–362.
104 J. D. Hunter, *Comput. Sci. Eng.*, 2007, **9**, 90–95.
105 R. Moos and K. H. Härdtl, *J. Am. Ceram. Soc.*, 1997, **80**, 2549–2562.
106 M. Knight, I. Reimanis, A. Meyer, J.-H. Preusker and W. Rheinheimer, *J. Am. Ceram. Soc.*, 2023, **106**, 4740–4751.

107 C.-J. Shin, H.-I. Yoo and C.-E. Lee, *Solid State Ion.*, 2007, **178**, 1081–1087.
108 R. A. De Souza, F. Gunkel, S. Hoffmann-Eifert and R. Dittmann, *Phys. Rev. B: Condens. Matter Mater. Phys.*, 2014, **89**, 241401.
109 G. M. Choi and H. L. Tuller, *J. Am. Ceram. Soc.*, 1988, **71**, 201–205.
110 H.-I. Yoo and K. D. Becker, *Phys. Chem. Chem. Phys.*, 2005, **7**, 2068–2073.
111 F. Horikiri, N. Iizawa, L. Han, K. Sato, K. Yashiro, T. Kawada and J. Mizusaki, *Solid State Ion.*, 2008, **179**, 2335–2344.
112 R. A. De Souza, *Adv. Funct. Mater.*, 2015, **25**, 6326–6342.
113 R. Waser, T. Bieger and J. Maier, *Solid State Commun.*, 1990, **76**, 1077–1081.
114 D. M. Smyth, *Curr. Opin. Solid State Mater. Sci.*, 1996, **1**, 692–697.
115 A. Klein, K. Albe, N. Bein, O. Clemens, K. A. Creutz, P. Erhart, M. Frericks, E. Ghorbani, J. P. Hofmann and B. Huang, *et al.*, *J. Electroceram.*, 2023, 1–31.
116 P. C. McIntyre, *J. Am. Ceram. Soc.*, 2000, **83**, 1129–1136.
117 R. A. De Souza and E. C. Dickey, *Philos. Trans. R. Soc. A*, 2019, **377**, 20180430.
118 A. H. H. Ramadan and R. A. De Souza, *Acta Mater.*, 2016, **118**, 286–295.
119 C. Tao, D. Mutter, D. F. Urban and C. Elsässer, *Phys. Rev. B*, 2021, **104**, 054114.
120 D. Mutter, C. Tao, D. F. Urban and C. Elsässer, *Adv. Eng. Mater.*, 2023, 2201847.
121 H. E. Weaver, *J. Phys. Chem. Solids*, 1959, **11**, 274–277.
122 G. Rupprecht and R. O. Bell, *Phys. Rev.*, 1964, **135**, A748.
123 T. Sakudo and H. Unoki, *Phys. Rev. Lett.*, 1971, **26**, 851.
124 R. A. Van der Berg, P. W. M. Blom, J. F. M. Cillessen and R. M. Wolf, *Appl. Phys. Lett.*, 1995, **66**, 697–699.
125 M. Trainer, *Eur. J. Phys.*, 2000, **21**, 459.
126 S. A. Prosandeev, A. E. Maslennikov, W. Kleemann and J. Dec, *Ferroelectrics*, 2000, **238**, 171–178.
127 J. Maier, *Phys. Chem. Chem. Phys.*, 2009, **11**, 3011–3022.
128 M. Gouy, *J. Phys. Theor. Appl.*, 1910, **9**, 457–468.
129 D. L. Chapman, *Lond. Edinb. Dublin Philos. Mag. J. Sci.*, 1913, **25**, 475–481.
130 W. Schottky, *Z. Phys.*, 1939, **113**, 367–414.
131 W. Schottky and E. Spenke, *Wissenschaftliche Veröffentlichungen aus den Siemens-Werken*, 1939, **18**, 225–291.
132 N. F. Mott, *Proc. R. Soc. London, Ser. A*, 1939, **171**, 27–38.
133 O. Kienzle, M. Exner and F. Ernst, *Phys. Status Solidi A*, 1998, **166**, 57–71.
134 S. Hutt, O. Kienzle, F. Ernst and M. Rühle, *Z. Metallkd.*, 2001, **92**, 105–109.
135 R. E. Mistler and R. L. Coble, *J. Appl. Phys.*, 1974, **45**, 1507–1509.
136 K. D. Chowdhury, R. Carpenter and W. Braue, *Ultramicroscopy*, 1992, **40**, 229–239.
137 H. Gu and Y. Shinoda, *Interface Sci.*, 2000, **8**, 269–278.
138 W. G. Morris, *J. Vac. Sci. Technol.*, 1976, **13**, 926–931.
139 T. Van Dijk and A. J. Burggraaf, *Phys. Status Solidi A*, 1981, **63**, 229–240.
140 J. P. Parras and R. A. De Souza, *Acta Mater.*, 2020, **195**, 383–391.
141 H. Yang, P. G. Kotula, Y. Sato, M. Chi, Y. Ikuhara and N. D. Browning, *Mater. Res. Lett.*, 2014, **2**, 16–22.
142 J. Jamnik and J. Maier, *Phys. Chem. Chem. Phys.*, 2001, **3**, 1668–1678.
143 Z. A. Munir, U. Anselmi-Tamburini and M. Ohyanagi, *J. Mater. Sci.*, 2006, **41**, 763–777.
144 O. Guillon, J. Gonzalez-Julian, B. Dargatz, T. Kessel, G. Schierning, J. Räthel and M. Herrmann, *Adv. Eng. Mater.*, 2014, **16**, 830–849.
145 M. Cologna, B. Rashkova and R. Raj, *J. Am. Ceram. Soc.*, 2010, **93**, 3556–3559.
146 M. Shirpour, G. Gregori, L. Houben, R. Merkle and J. Maier, *Solid State Ion.*, 2014, **262**, 860–864.
147 J. Bae, Y. Lim, J.-S. Park, D. Lee, S. Hong, J. An and Y.-B. Kim, *J. Electrochem. Soc.*, 2016, **163**, F919.
148 G. Dezanneau, A. Morata, A. Tarancón, M. Salleras, F. Peiró and J. R. Morante, *Appl. Phys. Lett.*, 2006, **88**, 141920.
149 G. Dezanneau, A. Morata, A. Tarancón, F. Peiró and J. R. Morante, *Solid State Ion.*, 2006, **177**, 3117–3121.
150 T. Bondevik, J. M. Polfus and T. Norby, *Solid State Ion.*, 2020, **353**, 115369.
151 V. Ravikumar, R. P. Rodrigues and V. P. Dravid, *Phys. Rev. Lett.*, 1995, **75**, 4063.
152 Y. G. Wang and V. P. Dravid, *Philos. Mag. Lett.*, 2002, **82**, 425–432.

